Article

Model to Link Cell Shape and Polarity with Organogenesis

Cell wedging & intercalation

Budding

α

α

Polarized particles

Gastrulation

Neurulation

Bjarke Frost Nielsen, Silas Boye Nissen, Kim Sneppen, Joachim Mathiesen, Ala Trusina

mathies@nbi.ku.dk (J.M.)
trusina@nbi.ku.dk (A.T.)

HIGHLIGHTS
Cell wedging and intercalation are modeled using a polarized point-particle approach

Cell intercalation is sufficient for tube budding

Tube budding is more robust when intercalation is complemented by wedging

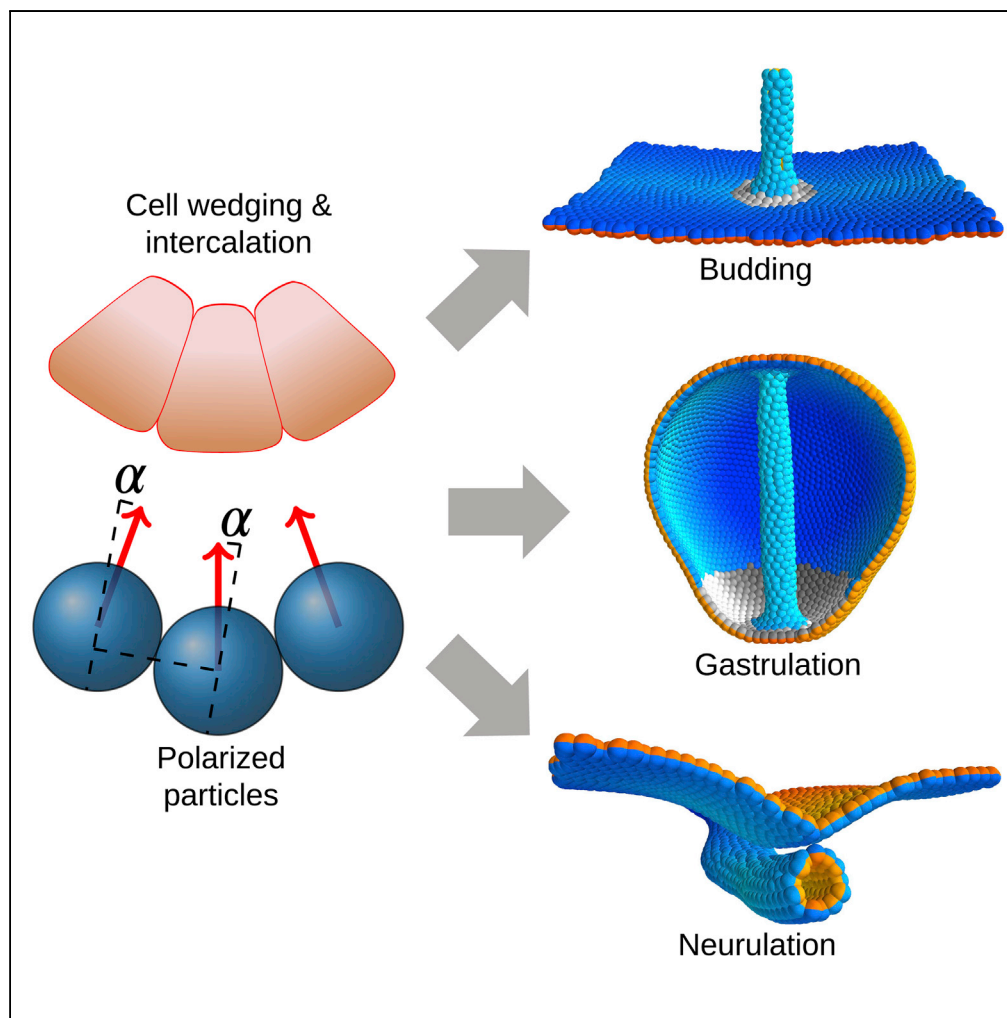Wedging and differential proliferation are sufficient for mammalian neurulation

Article

Model to Link Cell Shape and Polarity with Organogenesis

Bjarke Frost Nielsen,[1] Silas Boye Nissen,[1] Kim Sneppen,[1] Joachim Mathiesen,[1,*] and Ala Trusina[1,2,*]

SUMMARY

How do flat sheets of cells form gut and neural tubes? Across systems, several mechanisms are at play: cells wedge, form actomyosin cables, or intercalate. As a result, the cell sheet bends, and the tube elongates. It is unclear to what extent each mechanism can drive tube formation on its own. To address this question, we computationally probe if one mechanism, either cell wedging or intercalation, may suffice for the entire sheet-to-tube transition. Using a physical model with epithelial cells represented by polarized point particles, we show that either cell intercalation or wedging alone can be sufficient and that each can both bend the sheet and extend the tube. When working in parallel, the two mechanisms increase the robustness of the tube formation. The successful simulations of the key features in *Drosophila* salivary gland budding, sea urchin gastrulation, and mammalian neurulation support the generality of our results.

INTRODUCTION

Early tubes in embryonic development—gut and neural tubes—form out of epithelial sheets. In mammalian neurulation and *Drosophila* gastrulation, the cell sheet wraps around the tube axis until the edges make contact and fuse. As a result of such *wrapping*, a tube is formed parallel to the cell layer. In sea urchin, the gut is formed orthogonal to the epithelial plane by *budding* out of the plane. Budding also appears to be a predominant form of tube formation in organ development (lungs and kidneys in vertebrates, salivary gland, and trachea in *Drosophila* [Andrew and Ewald, 2010]). The same key mechanisms drive both wrapping and budding sheet-to-tube transitions: changes in cell shape, contracting myosin cables spanning across cells, and convergent extension (CE) by directed cell intercalation (Andrew and Ewald, 2010; Chung et al., 2017). Cells change their shapes by adjusting their apical surfaces relative to their basal surfaces—apical constriction (AC) (Sawyer et al., 2010) or basal constriction (Gutzman et al., 2018; Visetsouk et al., 2018). In the following, we will refer to apical or basal constriction as *wedging* and directed cell intercalation as CE. In addition, oriented cell division and spatially restricted apoptosis (Andrew and Ewald, 2010) contribute to tubulogenesis in other systems.

Until recently, the consensus has been that wedging and CE each lead to distinct morphological transformations: wedging bends the sheet, and CE elongates the sheet and the eventual tube (Andrew and Ewald, 2010). Over decades, wedging was assumed to be a primary mechanism for invagination in budding (Paluch and Heisenberg, 2009). However, results by Sanchez-Corrales et al. (2018) show that wedging and radial CE are coupled, and both contribute to the invagination in *Drosophila* salivary gland. Furthermore, Nishimura et al. (2012) argue that in mammalian neurulation, CE and wedging are coupled through planar cell polarity (PCP). First, the direction of cell intercalations, orthogonal to the tube axis, is set by PCP. Second, wedging must be anisotropic—with a preferred direction parallel to PCP and the direction of intercalation—for the sheet to wrap into a tube and not a spherical lumen. This anisotropy may stem from the coupling between PCP and wedging, apical as well as basal constriction. This is supported by data at the molecular level (for neural tube closure [Nishimura et al., 2012; Ossipova et al., 2014], the midbrain-hindbrain boundary in zebrafish [Gutzman et al., 2018; Visetsouk et al., 2018], and gastrulation in *C. elegans* [Lee et al., 2006], sea urchin [Croce et al., 2006], and *Xenopus* [Choi and Sokol, 2009]). Although the role of anisotropic wedging has been well characterized in *Drosophila* gastrulation (Chanet et al., 2017; Guglielmi et al., 2015; Martin et al., 2010; Sweeton et al., 1991), the origins of the anisotropy are still being debated (Doubrovinski et al., 2018).

The recent developments open for new questions: *What are wedging and CE capable of on their own? Can invagination happen by CE alone? Is anisotropy in wedging essential for tubulogenesis, and, if so, when?*

[1]Niels Bohr Institute, University of Copenhagen, Blegdamsvej 17, 2100 Copenhagen, Denmark

[2]Lead Contact

*Correspondence: mathies@nbi.ku.dk (J.M.), trusina@nbi.ku.dk (A.T.)

In this paper, we introduce a theoretical model to address these questions. Theoretical models have been essential for understanding tubulogenesis. However, they are often limited to 2D and thus focus on either wedging or CE (Belmonte et al., 2016; Collinet et al., 2015; Spahn and Reuter, 2013). Although there are 3D models for budding and neurulation (Inoue et al., 2016; Kim et al., 2013), they lack the coupling between planar polarization, wedging, and CE and do not capture the entire sheet-to-tube transition. To close this gap, we introduce a model of polarized cell-cell interactions where cells are treated as point particles. As a starting point, we consider the model suggested in Nissen et al. (2018), which was used to study polarized adhesion. We use term *polarized adhesion* to refer to the cell-cell interaction where adhesion proteins are either apicobasally polarized (AB) or planar polarized by, e.g., PCP. The model parts describing PCP are not limited to the PCP pathway but can be applied to systems where planar polarity is induced by other pathways (e.g., polarized Baz/Par3 in Drosophila germband extension [Paré et al., 2014] or salivary gland budding [Sanchez-Corrales et al., 2018]). The model in Nissen et al. (2018), however, could not explicitly account for changes in cell shapes. Here, we show that the effect of cell wedging can be very simply modeled within a point-particle representation by modifying cell-cell forces to favor a tilt in AB polarities.

In line with the proposition by Chung et al. (2017), simulations show that, although CE alone can lead to a budding transition, it is less reliable, with frequent failure of invagination and even evagination. Our results suggest that isotropic wedging orients the budding process and allows for robust invagination. When applied to wrapping in neurulation, we find that anisotropic wedging alone was insufficient for final tube closure. However, closure as well as tube separation from the epithelium can be aided by differential proliferation. Furthermore, we find that anisotropic wedging on its own may be sufficient for tube elongation. Together, our results support the mutual complementarity of wedging and CE in bending and elongation.

RESULTS

To investigate the role of cell wedging in budding and wrapping, we aimed at capturing both isotropic and anisotropic (PCP-driven) wedging with as few parameters as possible.

Modeling Wedging of a Point Particle by Favoring Tilt in AB

Apical constriction leads to cell wedging and, as a consequence, the AB axes of neighboring cells become tilted toward the wedged cell (Figures 1B and 1C). In Nissen et al. (2018), a flat epithelial sheet was modeled by a cell-cell interaction force favoring parallel AB polarities in neighboring cells (Figure 1A, Equation S1 in the Transparent Methods). To model the effect of wedging, we modify the force to favor AB polarity vectors $\mathbf{p}_i$ in neighbor cells to tilt toward the wedged cell (Figures 1B and 1C). That is, when the force is calculated, we replace $\mathbf{p}_i$ by $\tilde{\mathbf{p}}_i$ (Equations 1–3).

$$\tilde{\mathbf{p}}_i = \mathbf{p}_i \quad \text{(for no wedging)}, \quad \text{(Equation 1)}$$

$$\tilde{\mathbf{p}}_i \propto \mathbf{p}_i - \alpha \hat{\mathbf{r}}_{ij} \quad \text{(for isotropic wedging)}, \quad \text{(Equation 2)}$$

$$\tilde{\mathbf{p}}_i \propto \mathbf{p}_i - \alpha \langle \hat{\mathbf{q}} \rangle_{ij} \quad \text{(for anisotropic wedging)}. \quad \text{(Equation 3)}$$

Here, $\hat{\mathbf{r}}_{ij}$ is the normalized displacement vector between cells i and j, whereas $\langle \hat{\mathbf{q}} \rangle_{ij}$ is the averaged PCP vector of the two interacting particles.

This change required only one parameter, α, setting the extent of the tilt (large α corresponds to pronounced wedging). If the wedging is isotropic, i.e., equally pronounced in all directions (Sanchez-Corrales et al., 2018), all neighbors to the wedged cell tend to tilt equally. In neurulation, the wedging is anisotropic: the wedging happens primarily parallel to the cell's PCP and perpendicular to the axis of the tube (Nishimura et al., 2012). To capture this PCP-directed anisotropy, we couple the direction of AB tilting to the orientation of the cell's PCP (Equation 3, Figure 1C). See the Transparent Methods section for details of the model and simulations.

Note that we aim only to capture the effects of wedging-PCP coupling and not the molecular mechanism. Also, in an attempt to generalize our results, we focus on a minimal set of conditions necessary for the outcome.

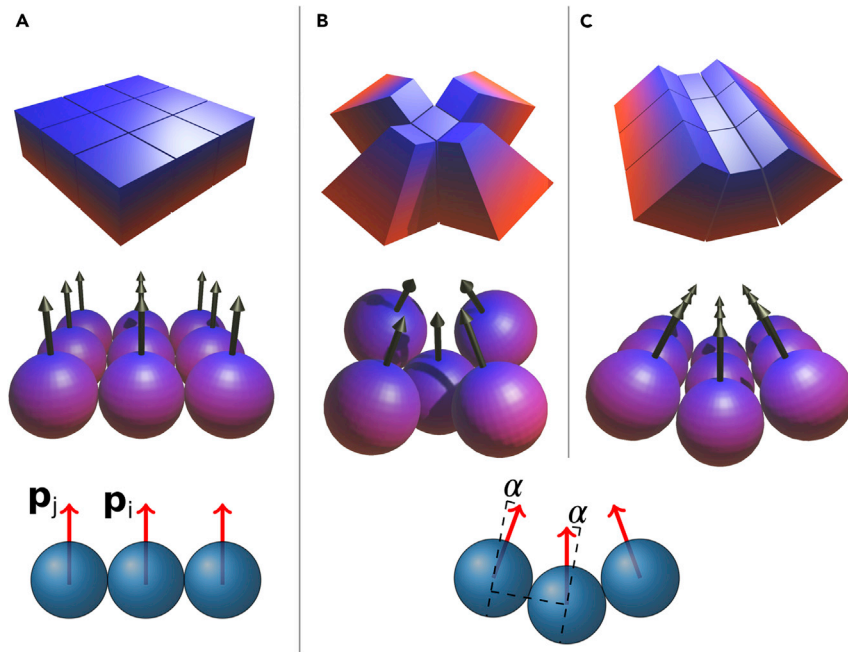We first consider the complementary roles of CE and wedging in budding.

Figure 1. Wedging Is Introduced through a Cell-Cell Interaction that Favors Tilted AB Polarity Vectors

α is the extent of wedging. The blue-red gradient indicates the apical-basal axis.

(A) No wedging ($\alpha = 0$), AB polarities (arrows) tend to be parallel.

(B) With isotropic wedging, the tilt α is the same in all directions.

(C) With anisotropic wedging, the tilt has a preferred direction. Blue and red signify, respectively, basal and apical surfaces. p_i and p_j are the AB polarities of cells i and j.

See also Figure S3 and S9, Video S1.

Complementary and Unique Roles of CE and Wedging in Budding

Results by Sanchez-Corrales et al. (2018) and Chung et al. (2017) suggest that both wedging and CE contribute to invagination. However, computational models have generally focused on either wedging as a driver for invagination or CE as a driver of tissue elongation (Belmonte et al., 2016; Collinet et al., 2015; Spahn and Reuter, 2013). To date, no computational models have managed to combine both mechanisms or probe the role of CE in invagination.

We set out to reproduce these experimental observations. The aim is to only capture the budding, leaving out the finer details of the *Drosophila* salivary gland, such as off-center invagination. We start with a flat sheet of AB polarized cells. Motivated by the possible link between organizing signals (e.g., WNT), PCP, and wedging (Habib et al., 2013; Loh et al., 2016), we define a region of "organizing signals" such that the cells within this region exhibit isotropic wedging and PCP. In *Drosophila* salivary glands, the apically constricting cells are distributed on a disk around the future center of the tube. With this configuration, we did not find parameters where both CE and wedging could act in parallel to form a well-defined tube Figures S8A–S8C. However, a ring of basally constricting cells remedied this problem and allowed for wedging and CE to act in parallel. This was the case whether a disk of apically constricting cells was included (Figures S8D–S8F) or not (Figure 2A). Supporting this, the data by Sanchez-Corrales et al. (2018) suggest that there are basally constricting cells in the outer region of the placode. Furthermore, basal and apical constriction seems to be induced by the same organizing signal (Gutzman et al., 2018) through PCP pathways. Also, in sea urchin gastrulation, both types of wedging seem to be at play (Kominami and Takata, 2004). For simplicity, we limit our simulations to basal wedging, where basally constricting cells are distributed on a ring (Figures 2A and S5).

Our budding simulations thus show that successful invagination and tube elongation can proceed if both wedging and PCP (and thus CE) act in parallel (Video S2, Figures 2A–2C). We have also succeeded in simulating sea urchin gastrulation where budding starts from a sphere of cells (Figure 3, Video S3, Kimberly and
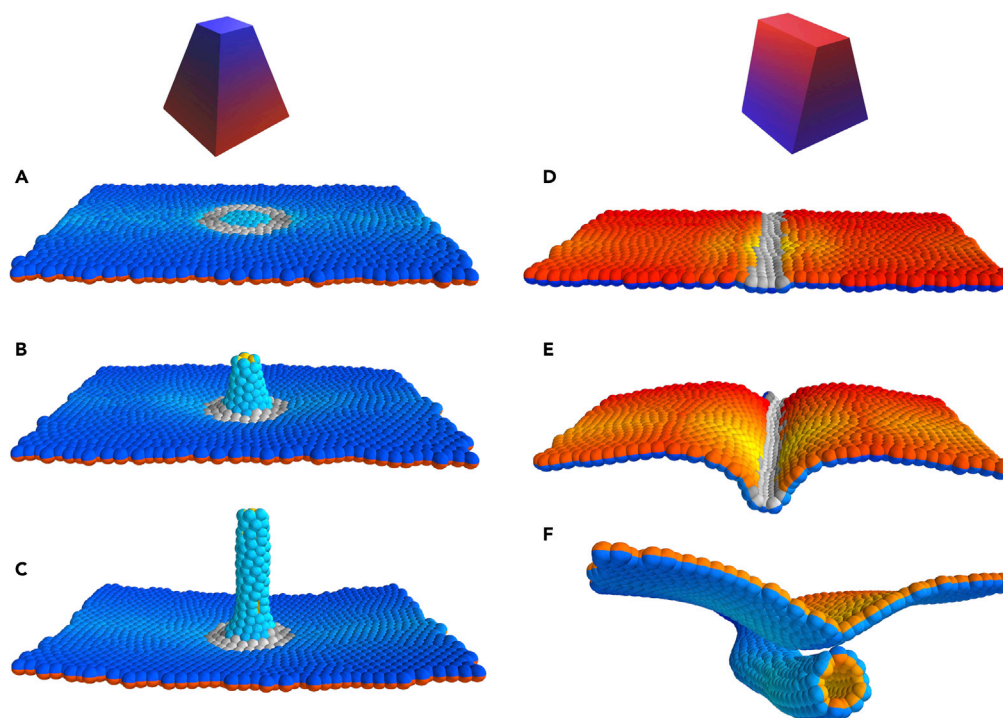
Figure 2. Isotropic and Anisotropic Wedging Drive Budding and Wrapping, Respectively

Wedging cells are labeled in gray, with a shading that indicates the PCP direction.

(A–C) Time evolution of budding simulation (similar to *Drosophila* salivary glands). Here, gray cells constrict basally and all cells on and inside the ring intercalate radially. The couplings are $(\lambda_1, \lambda_2, \lambda_3) = (0.5, 0.4, 0.1)$, the degree of wedging is $|\alpha| = 0.5$, and the annulus within which wedging occurs is given by the radii $r_0 = 5$ and $r_1 = 15$. See section *Modeling budding from a plane* for details, as well as Figure S5. Total number of time steps was 6.25×10^4 at $dt = 0.2$. Snapshots correspond to times 5, 800, and 1.25×10^4. The width of the Gaussian noise was $\sigma = 0.05$. See also Figures S1, S7, and S8, Video S2.

(D–F) Time evolution of wrapping simulation (similar to neurulation). Here, gray cells representing neuroepithelium constrict apically and constriction is anisotropic, follows the direction of PCP (Eq 3). Cells proliferate only at the gray/colored boundary (with 7-h doubling time), mimicking differential proliferation at the neuroepithelium/ectoderm boundary. The couplings are $(\lambda_1, \lambda_2, \lambda_3) = (0.6, 0.4, 0)$, the degree of wedging is $|\alpha| = 0.5$. See section *Modeling neurulation/wrapping* for details, as well as Figure S4.

Total number of time steps was 3.9×10^4 at $dt = 0.1$, and snapshots were taken at times 5, 900, and 3.9×10^3. The cell cycle length in simulation time units is 600. This simulation was run without added Gaussian noise, but noise is supplied by proliferation, which is implemented as a Poisson process. See also Videos S4 and S5.

Hardin, 1998; Lyons et al., 2012). This proceeds essentially like in the planar case (see Transparent Methods for details).

In addition, we find that budding *can* proceed without wedging if we allow for noise—random fluctuations in cell position and polarity orientation (Figure S1, Equation S4 in the Transparent Methods). Even slight noise, with a width of less than a tenth of a cell radius, breaks the symmetry between the two sides of the plane and initiates the CE-driven tubulation in one of the two directions orthogonal to the plane. However, the robustness of the outcome decreases in two ways. First, the proportion of failed invaginations is higher (Figure S1). Second, the tube can form on either side of the epithelial plane.

Thus, it seems that the role of wedging is to aid in the initial invagination and ensure correct orientation. Interestingly, in the mutants where wedging is compromised, Chung et al. (2017) observe that, despite initial invagination in the right direction, the tubes form less reliably and sometimes reorient in the wrong direction. Our results, showing complementary roles of CE and wedging, are thus in line with the findings by Sanchez-Corrales et al. (2018) and Chung et al. (2017).
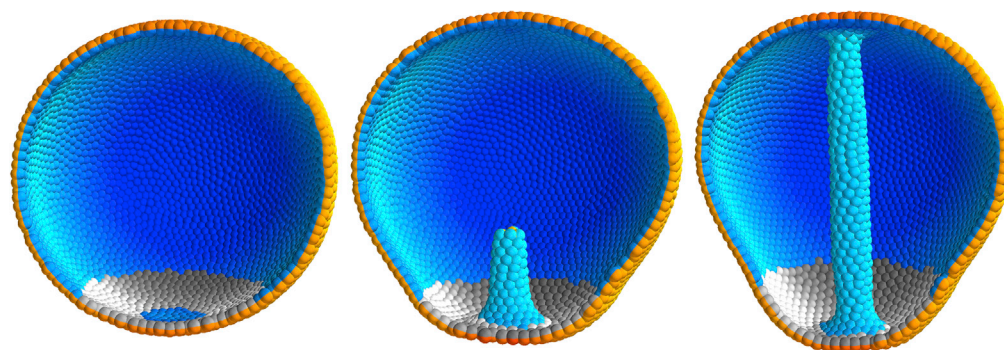
Figure 3. Isotropic Wedging in Conjunction with PCP Is Sufficient to Drive Sea Urchin Gastrulation without External Forcing

The gray ring shows cells with (isotropic) basal constriction, and the shading indicates the direction of planar cell polarity, which curls around the vertical axis in our simulation. The couplings are $(\lambda_1, \lambda_2, \lambda_3) = (0.5, 0.4, 0.1)$, the degree of wedging is $|\alpha| = 0.4$, and the annulus within which wedging occurs is given by the radii $r_0 = 7$ and $r_1 = 21$. See section *Modeling gastrulation* for details. Total number of time steps was 1.25×10^5 at $dt = 0.1$ and snapshots were taken at times 5, 1.5×10^3, and 1.25×10^4. The width of the Gaussian noise was $\sigma = 0.05$.

See also Video S3.

Cell shape change, intercalation, and tissue compression by supracellular myosin cables are also critical players in wrapping (Nishimura et al., 2012). The differences that cause some tubes to form parallel and others to form orthogonal to the epithelial plane appear to be encoded in the geometrical arrangement of the cells that participate in these three processes. In budding, such cells are arranged on a ring or a disk (circular symmetry), whereas in wrapping, they are arranged on a band (axial symmetry).

Anisotropic Wedging and Differential Proliferation Are Sufficient for Wrapping

To test if this difference in geometry alone is sufficient for wrapping, we choose a stripe of cells in the middle of the epithelial sheet to represent the neuroepithelium (NE) (shown as gray in Figures 2D and 2E) and the remaining cells to represent ectoderm (E) (colored cells in Figures 2D–2F). The NE cells are then assigned anisotropic apical constriction and PCP pointing orthogonal to the future tube axis (Figure S4).

Wrapping Requires Anisotropy in Wedging

In the case of isotropic wedging, one would expect a collection of NE cells to eventually form a round invagination or spherical lumen—the minimum energy state (Video S1). If we impose isotropic wedging in our neurulation simulations, we obtain a bulging, rounded invagination, rather than a tube. See Video S4.

Motivated by the results of Nishimura et al. (2012), showing that wedging is anisotropic (Equation 3) and cells wedge primarily in the direction orthogonal to the tube axis, we asked if anisotropic wedging can aid in tube closure. As expected, the tissue bends around the tube axis without capping at the ends of the tube (Figures 1C and S2).

Interestingly, anisotropic wedging also leads to cell intercalation by CE, narrowing, and elongating neuroepithelium (see Figure S3), thus supporting the link between PCP-driven wedging and cell intercalations. The simple, intuitive argument for this comes from how wedged cells pack in the tube. In the minimum energy state, the extent of wedging, α, determines how many cells can pack around the circumference of the tube (Figures 1 and S9). If the cells do not change in size, fewer cells are needed to close the circumference as wedging increases. If there are more cells than the wedging can allow for, the "extra" cells will be displaced (to minimize energy). Because of the forces mediated by AB polarity (e.g., tight junctions), cells are constrained to move within the epithelium and are, as a result, displaced along the tube axis (Figure S3). CE-driven narrowing of the epithelium was proposed as necessary for tube closure (Wallingford et al., 2002). In our simulations, wedging and CE alone succeeded in bending the tissue in an axially symmetric fashion (Figure S2). However, we could not obtain successful tube closure even with maximal possible
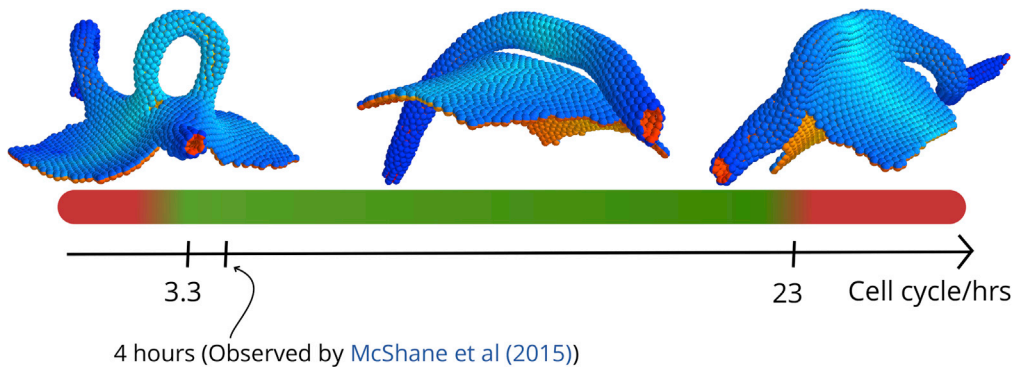
Figure 4. The Cell Cycle Length at the Neuroepithelial-Ectoderm Boundary Affects Tube Closure
For cell cycle lengths below 3.3 h and above 23 h the neural tube fails to close in our simulations. It should be noted that this broad interval also contains the cell cycle length of 4 h found for cells in the dorsolateral hinge points by McShane et al. (2015). The insets show outcomes of simulations run at short (2.6 h), intermediate (12 h), and long (26 h) cell cycle lengths. In simulation time, these correspond to 400, 1,800, and 4,000, respectively. See also Figures S2 and S6.

CE and wedging (both tuned by the strength of α in Equation 3). This suggests that additional mechanisms are necessary for final tube closure.

Buckling by Proliferation at the NE Boundary Aids in Tube Closure

Images of neurulation cross-sections (see e.g., Galea et al. [2018]) show a sharp bending at the neuroepithelium-ectoderm (NE-E) boundary, with a curvature opposite to that inside the neuroepithelium (neural folds) (Smith and Schoenwolf, 1997). This is believed to be a result of combined forces from the ectoderm due to (1) change in cell shape (ectoderm cells become flatter and neuroepithelial cells become taller); (2) adhesion between basal surfaces of NE and E close to the neuroepithelium-ectoderm (NE-E) boundary (Smith and Schoenwolf, 1997), and (3) increase in cell density at this boundary either due to cell proliferation or intercalation (McShane et al., 2015).

Our goal was to test if the model can capture full tube closure with at least one of the mechanisms, so for simplicity, we focused on differential proliferation. When cells were set to proliferate only at the NE-E boundary (McShane et al., 2015), we found that the resulting buckling can lead to successful neural tube closure (Video S5). In the simulations, the out-of-equilibrium buckling created by rapid cell proliferation is necessary to create a narrow neck that allows epithelial folds to fuse. We find that tubulation is possible within a rather broad range of cell cycles (3–16 h). Shorter *or* longer cell cycles resulted in open-tube morphologies reminiscent of neural tube defects such as spina bifida (Figure 4). In both cases, the folds are too far apart to fuse, but for different reasons. If proliferation is too slow, the folds are far apart because the buckling is too weak.

On the other hand, when proliferation is too fast, the sheet does not have time to equilibrate, and CE does not catch up in narrowing it. Because of this, some sections of the tube become too wide to fuse. Interestingly this can sometimes lead to tube doubling/splitting (Figure S6).

The effect of slow proliferation in our simulations is in line with the experimental data. In Copp et al. (1988), it was shown that low proliferation rates could lead to neural tube defects in mice. In humans, mutations of the PAX3 transcription factor are implicated in Waardenburg syndrome (Baldwin et al., 1994; Tassabehji et al., 1993) characterized by incomplete neural tube closure. The same transcription factor is essential in ensuring sufficient cell proliferation (Wu et al., 2015). The effect of increased (compared with wild-type) proliferation has not been addressed experimentally, and we hope that our predictions will motivate experiments in this direction.

DISCUSSION

Larger organisms rely on tubes for distributing nutrients across the body as well as for exocrine functions. How these tubes reliably form is an open question. A few recurrent mechanisms are known, e.g., directed

or differential proliferation, changes in cell shapes, supracellular myosin cables, polarized adhesion, and cell rearrangements. As evolution proceeds by tinkering rather than engineering, it is not surprising that these mechanisms have overlapping functions. Recently quantitative experiments (Chung et al., 2017; Nishimura et al., 2012; Sanchez-Corrales et al., 2018) enabled us to look beyond a "one mechanism, one function" relationship and toward a map of where mechanisms overlap and how they complement each other.

In this work, we have taken a step toward charting the functional overlap and complementarity among CE, wedging, and proliferation. A phenomenological point-particle representation allows us for the first time to combine PCP-driven cell intercalation (CE) and anisotropic wedging in thousands of cells in 3D and with a few free parameters. With this new tool we arrive at the following key results: First, our simulations show that CE can drive invagination in the absence of wedging, thus suggesting that this is a general mechanism that does not require forces from surrounding tissues. The invagination is, however, unreliable, and isotropic wedging plays a complementary role by setting the direction of invagination. The PCP pathway is not expressed in Drosophila salivary gland budding. One might therefore question why modeling the effects of planar polarity—and its role for CE—is valid in this system. However, despite differences at the molecular level, similarities emerge at the cellular level. At the cellular level, planar polarized adhesion is ubiquitous in systems undergoing CE: In mammalian neurulation, the adhesion protein Celsr is planar polarized by PCP (Nishimura et al., 2012); in early Drosophila development, Baz/Par3 is also planar polarized (by Toll receptors in gastrulation [Paré et al., 2014] and by unknown sources in salivary glands [Sanchez-Corrales et al., 2018]). Within our coarse-grained description of polar cell-cell interactions it is not necessary to differentiate whether the effects of planar polarization are due to PCP pathways or other sources, as long as polarized adhesion drives cell-cell intercalation. Also, we do not explicitly model the origins of planar polarity patterning, e.g., WNT signals orienting PCP (Humphries and Mlodzik, 2018) or Toll receptors orienting Baz/Par3 (Paré et al., 2014). Instead we pre-pattern the orientation of polarities directly. We can then either keep the orientation of planar polarities fixed, to simulate a global patterning by, e.g., Toll receptors, or let the global planar polarity pattern dynamically emerge from cell-cell interactions.

Second, our results predict that anisotropic, PCP-coupled wedging may play a role in tube formation and elongation. Our model predicts that anisotropy in wedging maintains axial symmetry of the tube during wrapping. Remarkably, anisotropic wedging can also lead to CE-like cell intercalation and, consequently, tube elongation. Although we have only tested the contribution of anisotropic wedging in wrapping, the same principle may apply in budding. In support of this, in budding, the initially isotropic wedging (Röper, 2012; Sanchez-Corrales et al., 2018) becomes anisotropic after the invagination, when the tube elongates (Pirraglia et al., 2010). Such an isotropic-to-anisotropic transition in wedging has been reported in Drosophila furrow formation (Leptin and Roth, 1994; Sweeton et al., 1991). Furthermore, visual inspection of tube cross-sections in the pancreas and kidneys suggests that cells are wedged. By analogy to neurulation, it is reasonable to expect wedging to be anisotropic in all tubes. It will be interesting to confirm this experimentally by, e.g., whole-mount 3D imaging of stained tubes.

Third, *differential proliferation* together with *anisotropic wedging* are sufficient for tube closure and separation in wrapping. Each of the mechanisms has to be spatially constrained. To buckle the cell sheet, proliferation must be faster at the neuroepithelium/ectoderm boundary than in the remaining tissue. Because only neuroepithelium forms the tube, anisotropic wedging must be localized to these cells. Differential proliferation has been proposed by McShane et al. (2015) as a mechanism for forming dorsolateral hinge points (DLHPs), regions where the tissue curvature has the same sign as at medial hinge points (MHPs). We find that modifying the extent of apical constriction or how it is distributed, i.e., throughout the entire neuroepithelium, or combinations of DLHPs and MHP, could not result in tube closure. Instead, our results highlight the importance of forming regions of opposite curvature at the boundaries. Our simulations suggest that differential proliferation buckles the boundaries and aids tube closure as it curves the epithelium oppositely to the curvature resulting from apical constriction.

Our simulations predict a wide range of proliferation rates capable of producing sufficient buckling for closure. These results call for testing for differential proliferation in systems without DLHPs (by accelerating or reducing proliferation rate in mutants or by molecular inhibitors [Li et al., 2017]). Although not

immediately feasible, it is also interesting to consider how to perturb the "opposite" curvature by interfering with differences in cell shapes or basal adhesion (Smith and Schoenwolf, 1997) of the neuroepithelium and ectoderm close to the boundary.

Models of tubulogenesis date back at least a few decades (Kerszberg and Changeux, 1998); however, most of them are limited to 2D and focus on either wedging or cell intercalation. Recently, Inoue et al. (2016) formulated a 3D vertex model of neurulation focusing on cell elongation, apical constriction, and active cell migration. The model does not include either cell proliferation or PCP but instead relies on active cell migration to pull the neural cells toward the midline. Although successful in bringing folds sufficiently close, it does not cover the separation of the tube from the sheet. In another system, the experimental and 3D modeling results by Osterfield et al. (2013) suggest that CE may be important in the early budding of the eggshell appendage. In their model, however, the initial invagination was driven by pre-patterned tension in the epithelium and neither cell polarity nor wedging were considered. Also, a recent 3D model of tube budding in the lung epithelium concluded that wedging can only result in rounded tubes and that it is insufficient to drive the entire process (Kim et al., 2013). Still, in that study, only isotropic wedging was considered. In our simulations, we see that anisotropy is necessary for tube formation.

We have demonstrated that cell wedging can be phenomenologically captured in a point-particle representation. This is not restricted to apical constriction but also covers, e.g., basal constriction, and can, in a similar spirit, be extended to capture changes in cell height and width. Also, adding oriented cell proliferation and local apoptosis is straight forward and could allow for modeling a wider range of tubulogenesis phenomena. Furthermore, we are now in a position to address tube branching in, e.g., lungs and vascularization, where cells forming the tubes also are the ones that secrete organizing signals that locally re-orient PCP polarities and may induce anisotropic changes in cell shapes.

Limitations of Study

A major limitation of our study is that we do not model the coupling of polarities to orienting morphogens (e.g., WNT, FGF, or BMP).

As a consequence, cell properties such as expression of apical-basal and planar cell polarity (and the orientation of polarities in individual cells) had to be assigned at the start of simulations. Furthermore, in the case of budding, the orientation of PCP had to be maintained fixed through the entire sheet-to-tube transition. We anticipate that, by including the morphogen-polarity coupling, the right distribution of cell types and polarity directions will emerge without externally imposed constraints.

METHODS

All methods can be found in the accompanying Transparent Methods supplemental file.

DATA AND CODE AVAILABILITY

The source code for the simulations is available on GitHub (Nielsen, 2019).

SUPPLEMENTAL INFORMATION

Supplemental Information can be found online at https://doi.org/10.1016/j.isci.2020.100830.

ACKNOWLEDGMENTS

AUTHOR CONTRIBUTIONS

B.F.N. programmed and ran the model simulations and created figures; B.F.N., A.T., J.M., S.B.N., and K.S. outlined the paper, developed the model, contributed to discussions, and wrote the manuscript.

DECLARATION OF INTERESTS

The authors declare no competing interests.

REFERENCES

Andrew, D.J., and Ewald, A.J. (2010). Morphogenesis of epithelial tubes: Insights into tube formation, elongation, and elaboration. Dev. Biol. *341*, 34–55.

Baldwin, C.T., Lipsky, N.R., Hoth, C.F., Cohen, T., Mamuya, W., and Milunsky, A. (1994). Mutations in pax3 associated with waardenburg syndrome type i. Hum. Mutat. *3*, 205–211.

Belmonte, J.M., Swat, M.H., and Glazier, J.A. (2016). Filopodial-tension model of convergent-extension of tissues. PLoS Comput. Biol. *12*, e1004952.

Chanet, S., Miller, C.J., Vaishnav, E.D., Ermentrout, B., Davidson, L.A., and Martin, A.C. (2017). Actomyosin meshwork mechanosensing enables tissue shape to orient cell force. Nat. Commun. *8*, 15014.

Choi, S.-C., and Sokol, S.Y. (2009). The involvement of lethal giant larvae and wnt signaling in bottle cell formation in xenopus embryos. Dev. Biol. *336*, 68–75.

Chung, S., Kim, S., and Andrew, D.J. (2017). Uncoupling apical constriction from tissue invagination. eLife *6*, e22235.

Collinet, C., Rauzi, M., Lenne, P.-F., and Lecuit, T. (2015). Local and tissue-scale forces drive oriented junction growth during tissue extension. Nat. Cell Biol. *17*, 1247.

Copp, A.J., Brook, F.A., and Roberts, H.J. (1988). A cell-type-specific abnormality of cell proliferation in mutant (curly tail) mouse embryos developing spinal neural tube defects. Development *104*, 285–295.

Croce, J., Duloquin, L., Lhomond, G., McClay, D.R., and Gache, C. (2006). Frizzled5/8 is required in secondary mesenchyme cells to initiate archenteron invagination during sea urchin development. Development *133*, 547–557.

Doubrovinski, K., Tchoufag, J., and Mandadapu, K. (2018). A simplified mechanism for anisotropic constriction in Drosophila mesoderm. Development *145*, dev167387. https://dev.biologists.org/content/145/24/dev167387.

Galea, G.L., Nychyk, O., Mole, M.A., Moulding, D., Savery, D., Nikolopoulou, E., Henderson, D.J., Greene, N.D., and Copp, A.J. (2018). Vangl2 disruption alters the biomechanics of late spinal neurulation leading to spina bifida in mouse embryos. Dis. Model. Mech. *11*, dmm032219.

Guglielmi, G., Barry, J.D., Huber, W., and De Renzis, S. (2015). An optogenetic method to modulate cell contractility during tissue morphogenesis. Dev. Cell *35*, 646–660.

Gutzman, J.H., Graeden, E., Brachmann, I., Yamazoe, S., Chen, J.K., and Sive, H. (2018). Basal constriction during midbrain–hindbrain boundary morphogenesis is mediated by wnt5b and focal adhesion kinase. Biol. Open *7*, bio034520.

Habib, S.J., Chen, B.-C., Tsai, F.-C., Anastassiadis, K., Meyer, T., Betzig, E., and Nusse, R. (2013). A localized wnt signal orients asymmetric stem cell division in vitro. Science *339*, 1445–1448.

Humphries, A.C., and Mlodzik, M. (2018). From instruction to output: wnt/pcp signaling in development and cancer. Curr. Opin. Cell Biol. *51*, 110–116.

Inoue, Y., Suzuki, M., Watanabe, T., Yasue, N., Tateo, I., Adachi, T., and Ueno, N. (2016). Mechanical roles of apical constriction, cell elongation, and cell migration during neural tube formation in xenopus. Biomech. Model. Mechanobiol. *15*, 1733–1746.

Kerszberg, M., and Changeux, J.-P. (1998). A simple molecular model of neurulation. BioEssays *20*, 758–770.

Kim, H.Y., Varner, V.D., and Nelson, C.M. (2013). Apical constriction initiates new bud formation during monopodial branching of the embryonic chicken lung. Development *140*, 3146–3155.

Kimberly, E.L., and Hardin, J. (1998). Bottle cells are required for the initiation of primary invagination in the sea urchin embryo. Dev. Biol. *204*, 235–250.

Kominami, T., and Takata, H. (2004). Gastrulation in the sea urchin embryo: a model system for analyzing the morphogenesis of a monolayered epithelium. Dev. Growth Differ. *46*, 309–326.

Lee, J.-Y., Marston, D.J., Walston, T., Hardin, J., Halberstadt, A., and Goldstein, B. (2006). Wnt/frizzled signaling controls *C. elegans* gastrulation by activating actomyosin contractility. Curr. Biol. *16*, 1986–1997.

Leptin, M., and Roth, S. (1994). Autonomy and non-autonomy in Drosophila mesoderm determination and morphogenesis. Development *120*, 853–859.

Li, Y., Muffat, J., Omer, A., Bosch, I., Lancaster, M.A., Sur, M., Gehrke, L., Knoblich, J.A., and Jaenisch, R. (2017). Induction of expansion and folding in human cerebral organoids. Cell Stem Cell *20*, 385–396.

Loh, K.M., van Amerongen, R., and Nusse, R. (2016). Generating cellular diversity and spatial form: wnt signaling and the evolution of multicellular animals. Dev. Cell *38*, 643–655.

Lyons, D.C., Kaltenbach, S.L., and McClay, D.R. (2012). Morphogenesis in sea urchin embryos: linking cellular events to gene regulatory network states. Wiley Interdiscip. Rev. Dev. Biol. *1*, 231–252.

Martin, A.C., Gelbart, M., Fernandez-Gonzalez, R., Kaschube, M., and Wieschaus, E.F. (2010). Integration of contractile forces during tissue invagination. J. Cell Biol. *188*, 735–749.

McShane, S.G., Molè, M.A., Savery, D., Greene, N.D., Tam, P.P., and Copp, A.J. (2015). Cellular basis of neuroepithelial bending during mouse spinal neural tube closure. Dev. Biol. *404*, 113–124.

Nielsen, B.F. (2019). OrganogenesisPCP. https://github.com/BjarkeFN/OrganogenesisPCP.

Nishimura, T., Honda, H., and Takeichi, M. (2012). Planar cell polarity links axes of spatial dynamics in neural-tube closure. Cell *149*, 1084–1097.

Nissen, S.B., Rønhild, S., Trusina, A., and Sneppen, K. (2018). Theoretical tool bridging cell polarities with development of robust morphologies. eLife *7*, e38407.

Ossipova, O., Kim, K., Lake, B.B., Itoh, K., Ioannou, A., and Sokol, S.Y. (2014). Role of rab11 in planar cell polarity and apical constriction during vertebrate neural tube closure. Nat. Commun. *5*, 3734.

Osterfield, M., Du, X., Schüpbach, T., Wieschaus, E., and Shvartsman, S.Y. (2013). Three-dimensional epithelial morphogenesis in the developing Drosophila egg. Dev. Cell *24*, 400–410.

Paluch, E., and Heisenberg, C.-P. (2009). Biology and physics of cell shape changes in development. Curr. Biol. *19*, R790–R799.

Paré, A.C., Vichas, A., Fincher, C.T., Mirman, Z., Farrell, D.L., Mainieri, A., and Zallen, J.A. (2014). A positional toll receptor code directs convergent extension in Drosophila. Nature *515*, 523.

Pirraglia, C., Walters, J., and Myat, M.M. (2010). Pak1 control of e-cadherin endocytosis regulates salivary gland lumen size and shape. Development *137*, 4177–4189.

Röper, K. (2012). Anisotropy of crumbs and apkc drives myosin cable assembly during tube formation. Dev. Cell *23*, 939–953.

Sanchez-Corrales, Y.E., Blanchard, G.B., and Röper, K. (2018). Radially patterned cell behaviours during tube budding from an epithelium. eLife *7*, e35717.

Sawyer, J.M., Harrell, J.R., Shemer, G., Sullivan-Brown, J., Roh-Johnson, M., and Goldstein, B. (2010). Apical constriction: a cell shape change that can drive morphogenesis. Dev. Biol. *341*, 5–19.

Smith, J.L., and Schoenwolf, G.C. (1997). Neurulation: coming to closure. Trends Neurosci. *20*, 510–517.

Spahn, P., and Reuter, R. (2013). A vertex model of drosophila ventral furrow formation. PLoS One *8*, e75051.

Sweeton, D., Parks, S., Costa, M., and Wieschaus, E. (1991). Gastrulation in Drosophila: the formation of the ventral furrow and posterior midgut invaginations. Development *112*, 775–789.

Tassabehji, M., Read, A.P., Newton, V.E., Patton, M., Gruss, P., Harris, R., and Strachan, T. (1993). Mutations in the pax3 gene causing waardenburg syndrome type 1 and type 2. Nat. Genet. *3*, 26.

Visetsouk, M.R., Falat, E.J., Garde, R.J., Wendlick, J.L., and Gutzman, J.H. (2018). Basal epithelial tissue folding is mediated by differential

regulation of microtubules. Development *145*, dev167031.

Wallingford, J.B., Fraser, S.E., and Harland, R.M. (2002). Convergent extension: the molecular control of polarized cell movement during embryonic development. Dev. Cell *2*, 695–706.

Wu, T.-F., Yao, Y.-L., Lai, I.-L., Lai, C.-C., Lin, P.-L., and Yang, W.-M. (2015). Loading of pax3 to mitotic chromosomes is mediated by arginine methylation and associated with Waardenburg syndrome. J. Biol. Chem. *290*, 20556–20564.

Supplemental Information

Model to Link Cell Shape

and Polarity with Organogenesis

Bjarke Frost Nielsen, Silas Boye Nissen, Kim Sneppen, Joachim Mathiesen, and Ala Trusina

Supplementary Figures

Figure S1   Budding outcomes in the absence of wedging. Related to Fig 2.

|	Normal	Failed	Misoriented
High Noise $\sigma = 0.1$ $N = 50$	40%	0%	60%
Low Noise $\sigma = 0.002$ $N = 50$	20%	50%	30%
No Noise $\sigma = 0$ $N = 50$	0%	100%	0%

Budding outcomes without wedging at high and low noise as well as in the absence of noise. The first column shows the proportion of normal initiations of tubulation, the middle column shows failed invaginations while the last column shows evaginations. σ is the width of the Gaussian noise, while N is the number of simulations run at the given noise level. See the Methods section for details on the implementation of noise. In all cases $dt = 0.1$. The couplings were kept at $(\lambda_1, \lambda_2, \lambda_3) = (0.4, 0.5, 0.1)$ and the annulus within which wedging occurs is given by the radii $r_0 = 5$ and $r_1 = 10$. Since wedging is absent, $\alpha = 0$.

Figure S2   Lack of proliferation. Related to Fig 4.
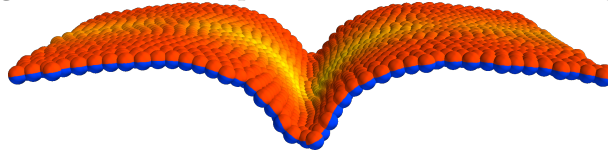

The fate of the neural sheet in our simulations in the absence of proliferation. Here the couplings are $(\lambda_1, \lambda_2, \lambda_3) = (0.6, 0.4, 0)$, the degree of wedging is $|\alpha| = 0.5$. See the section *Modeling neurulation/wrapping* for details. Total number of time steps was 1.4×10^5 at $dt = 0.1$. The simulation was run without noise.

**Figure S3   T1 transition induced by wedging. Related to Fig 1.**
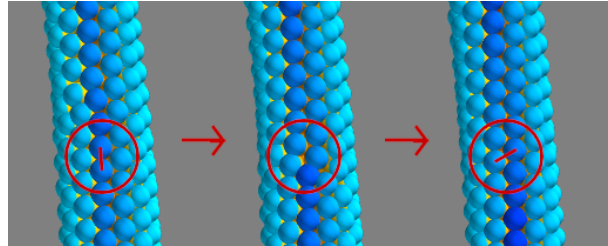
The T1 transition was induced by starting with a tube which was stabilized with anisotropic wedging of strength $|\alpha| = 0.3$ and then increasing the extent of wedging to $|\alpha| = 0.5$, causing the structure to tighten and elongate by intercalation. The couplings are $(\lambda_1, \lambda_2, \lambda_3) = (0.55, 0.45, 0)$ and the width of the Gaussian noise is 0.1 with time step size $dt = 0.2$.

Figure S4   The initial configuration of the cell sheet for neurulation. Related to Fig 2.
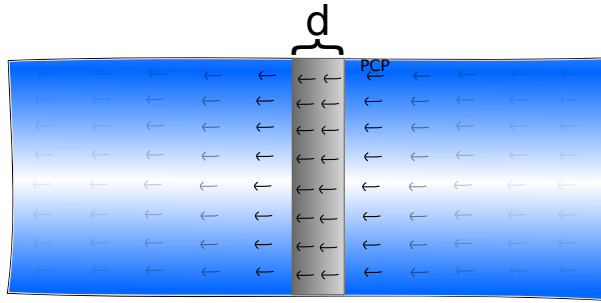
The initial configurations of the cell sheet for neurulation. Wedging is turned on in a band of width d (gray) with PCP running orthogonal to this band.

Figure S5   The initial configuration of the cell sheet for budding. Related to Fig 2.
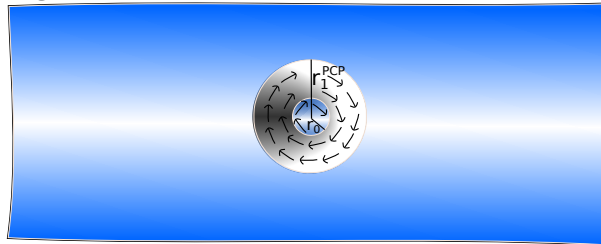
The initial configurations of the cell sheet for budding. Wedging is turned on in an annulus (gray) where PCP curls around tangentially.

Figure S6   Tube splitting observed with excessive proliferation rate. Related to Fig 4. The proliferation rate corresponds to a cell cycle length of 1.5h for cells at the neuroepithelium/ectoderm boundary. The remaining parameters are as in the main neurulation simulation, as described in Fig 2
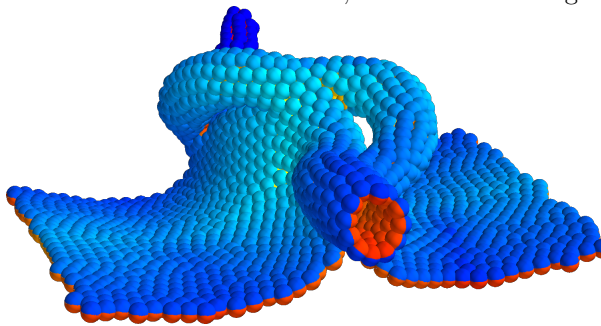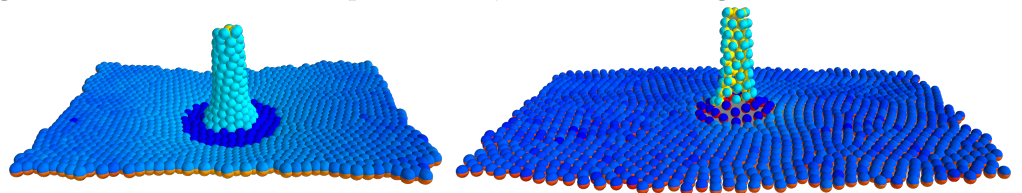

Figure S7   Influence of the parameter β. Related to Fig 2.

Budding simulations run with $\beta = 2.5$ (left) and $\beta = 10$ (right). This affects the equilibrium distance so that cells are closer together resp. further apart (and thus come across as larger resp. smaller) but budding progresses in a qualitatively similar manner.

The remaining simulations in this paper were all run with $\beta = 5$ ensuring an equilibrium distance of $d_{eq} = 2$.

Figure S8   Apical constriction in budding. Related to Fig 2.
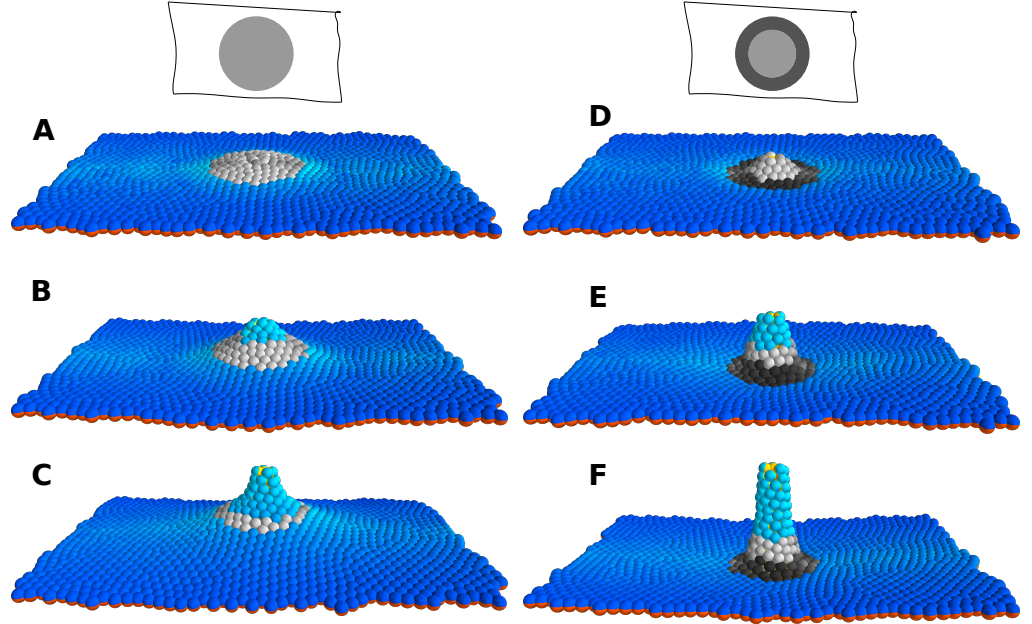
(**A-C**) Time evolution of budding simulation when only a disk of apically constricting cells (light gray) are assigned, and no basally contracting cells. The couplings are $(\lambda_1, \lambda_2, \lambda_3) = (0.5, 0.4, 0.1)$, the degree of wedging is $|\alpha| = 0.3$. The radius of the disk of apically constricting cells is given by $r_0 = 10$. Total number of time steps was 6.8×10^4 at $dt = 0.1$. Snapshots correspond to times 175, 600 and 6800.

(**D-F**) Time evolution of budding simulation when a disk of apically constricting cells (light gray) as well as a ring of basally constricting cells (dark gray) are assigned. The couplings are $(\lambda_1, \lambda_2, \lambda_3) = (0.5, 0.4, 0.1)$, the degree of wedging is $|\alpha| = 0.3$. The outer radius of the ring for which basal constriction occurs is given $r_1 = 10$ while the radius of the disk of apically constricting cells is given by $r_0 = 5$. Total number of time steps was 2.2×10^4 at $dt = 0.1$. Snapshots correspond to times 25, 400 and 2200.

Figure S9   The degree of wedging affects the circumference of the tube. Related to Fig 1.

Extent of cell wedging, α

Number of cells along circumference
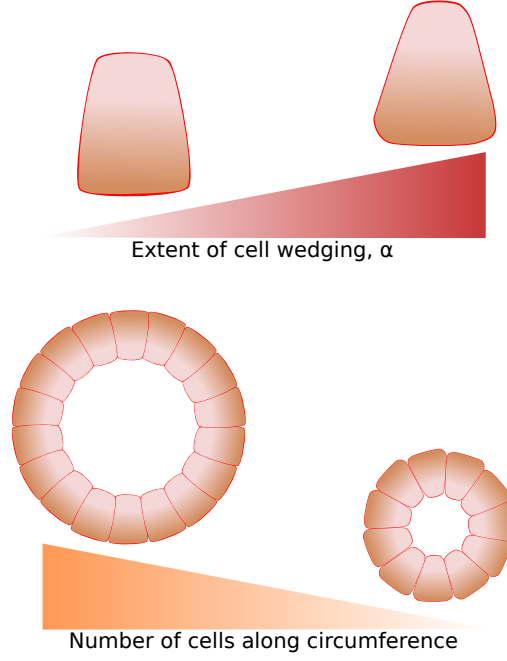
Transparent Methods

Model

Following Nissen et al. (2018), cells are treated as point particles interacting with neighboring cells through a pair-potential V_{ij}. The potential has a rotationally symmetric repulsive term and a polarity-dependent attractive term. In terms of r_{ij} (the distance between two cells i and j), the dimensionless potential can be formulated as

$$V_{ij} = e^{r_{ij}} - [\lambda_1 \, S_{ij}(A) + \lambda_2 \, S_{ij}(AP) + \lambda_3 \, S_{ij}(P)] \, e^{-r_{ij}/\beta}. \tag{S1}$$

The parameter β has the fixed value $\beta = 5$, since this ensures that the equilibrium distance is always 2, corresponding to 2 cell radii. In Figure S7 we have shown that one can obtain qualitatively similar results at other values of β. The parameters λ_i are coupling constants which define the strength of polar interactions in the model. $S_{ij}(A)$ gives the form of the interaction between AB polarity and position, whereas $S_{ij}(AP)$ and $S_{ij}(P)$ give the coupling of PCP with AB and position, respectively, as described in Nissen et al. (2018). These couplings are formulated in terms of AB vectors $\mathbf{p}_i$, PCP vectors $\mathbf{q}_i$ and a unit vector $\hat{\mathbf{r}}_{ij}$ from cell i to j. The coupling $S_{ij}(AP) = (\mathbf{p}_i \times \mathbf{q}_i) \cdot (\mathbf{p}_j \times \mathbf{q}_j)$ dynamically maintains the orthogonality of the PCP unit vectors $\mathbf{q}_i$ and $\mathbf{q}_j$ to their corresponding AB polarity vectors while lateral organization is favored by $S_{ij}(P) = (\hat{\mathbf{r}}_{ij} \times \mathbf{q}_i) \cdot (\hat{\mathbf{r}}_{ij} \times \mathbf{q}_j)$. In the absence of any cell shape effects, the coupling between AB and position is given by $S_{ij}(A) = (\hat{\mathbf{r}}_{ij} \times \mathbf{p}_i) \cdot (\hat{\mathbf{r}}_{ij} \times \mathbf{p}_j)$, which favors a flat cell sheet. Wedging of cells is introduced into our model by a single deformation parameter α, which describes an attractive interaction between the AB polarity unit vectors $\mathbf{p}_i$ and $\mathbf{p}_j$:

$$S_{ij}(A) = (\hat{\mathbf{r}}_{ij} \times \tilde{\mathbf{p}}_i) \cdot (\hat{\mathbf{r}}_{ij} \times \tilde{\mathbf{p}}_j), \tag{S2}$$

where $\tilde{\mathbf{p}}_i$ is given by

$$\tilde{\mathbf{p}}_i = \mathbf{p}_i \quad \text{(for no wedging)},$$

$$\tilde{\mathbf{p}}_i = \frac{\mathbf{p}_i - \alpha\hat{\mathbf{r}}_{ij}}{|\mathbf{p}_i - \alpha\hat{\mathbf{r}}_{ij}|} \quad \text{(for isotropic wedging)},$$

$$\tilde{\mathbf{p}}_i = \frac{\mathbf{p}_i - \alpha\left\langle\hat{\mathbf{q}}\right\rangle_{ij}}{|\mathbf{p}_i - \alpha\left\langle\hat{\mathbf{q}}\right\rangle_{ij}|} \quad \text{(for anisotropic wedging)}. \tag{S3}$$

Here, $\left\langle\hat{\mathbf{q}}\right\rangle_{ij}$ denotes the mean of PCP vectors $\mathbf{q}_i$ and $\mathbf{q}_j$ belonging to the two interacting cells. The above substitution, $\mathbf{p}_i \rightarrow \tilde{\mathbf{p}}_i$, is only performed in $S_{ij}(A)$, so as to only affect the coupling between AB polarity and position.

Setting $\alpha = 0$ favors a flat sheet (see Fig 1A–B) whereas a non-zero α favors bending of AB polarity vectors towards (or away from) one another and induces curvature in a sheet of cells (Fig 1C–D).

The time development is simulated by overdamped (relaxational) dynamics along the gradient of the above potential, Eq (S1):

$$\frac{\partial\mathbf{r}_i}{\partial t} = -\frac{\partial V_i}{\partial\mathbf{r}_i} + \eta,$$

$$\frac{\partial\mathbf{p}_i}{\partial t} = -\frac{\partial V_i}{\partial\mathbf{p}_i} + \eta,$$

$$\frac{\partial\mathbf{q}_i}{\partial t} = -\frac{\partial V_i}{\partial\mathbf{q}_i} + \eta, \tag{S4}$$

where the potential energy function for the i'th cell is $V_i = \sum_j V_{ij}$. The sum runs over those cells j which are within direct line of sight of the i'th cell as described in Nissen et al. (2018). η is a noise term corresponding to Gaussian white noise with vanishing mean. This noise term provides a degree of randomness to cell position as well as the orientation of polarities. Cell division (when present) is modeled as a Poisson process with daughter cells being placed randomly around the mother cell at a distance of one cell radius.

The model was implemented in Python using PyTorch for automatic differentiation (Paszke et al. 2017). Numerical integration of the equations of motion is implemented through the Euler method, usually with $dt = 0.1$. We have checked that the model converges to similar results (tested for budding) with $dt = 10^{-4}$. The source code for the simulations is available on GitHub (Nielsen 2019).

Parameter estimation and robustness

We have tested the robustness of our approach on a number of model cases and find that, for example, *budding* can be reproduced with a broad range of wedging parameters, $\alpha \in [0.1, 0.6]$ and for diverse PCP coupling strengths $\lambda_3 \in [0.8, 0.14]$. For these intervals, the budding is qualitatively similar to that illustrated in Fig 2A. Our typical values of wedging used in simulations, $\alpha \in [0.3, 0.5]$ are comparable with the wedging strains reported in Sanchez-Corrales et al. (2018), e.g. $0.03pp/\mu m$, corresponding to $\alpha = 0.4$ (assuming a cell diameter of 13μm) (Brown & Bron 1987).

We further explore our model by re-instating dimensions in the formulation of the potential and the equation of motion and estimating dimensionful quantities. With dimensions reinstated, the pair-potential takes the form

$$V_{ij} = V_0\left[\exp(-r/\ell) - S\exp(-r/(\beta\ell))\right]. \tag{S5}$$

The overdamped equation of motion (without noise) becomes

$$0 = \gamma \mathbf{v}_i + \frac{\partial V_{ij}}{\partial \mathbf{r}_i}, \tag{S6}$$

where $\mathbf{v}_i = \partial \mathbf{r}_i / \partial t$. We now introduce dimensionless (tilded) parameters

$$V_{ij} = V_0 \tilde{V}_{ij}, \quad \mathbf{r}_i = \ell \tilde{\mathbf{r}}_i, \quad v_i = v_0 \tilde{v}_i = \frac{\ell}{t_0} \tilde{v}_i. \tag{S7}$$

and insert the dimensionless parameters in our equation of motion

$$\tilde{\mathbf{v}}_i = -\frac{V_0}{\ell \gamma v_0} \frac{\partial \tilde{V}_{ij}}{\partial \tilde{\mathbf{r}}_i}. \tag{S8}$$

Inserting the dimensionless equation of motion, this reduces to $V_0 = \ell \gamma v_0$. In Eskandari & Salcudean (2008), a typical value for the dynamical viscosity μ was reported to be on the order of $250\,\mathrm{Pa\,s}$. This can be related to the coefficient γ by Stokes' Law of viscous drag, $\gamma = 6\pi\mu\ell$. We now compare our model with epithelial cell extrusion and use the typical cell speed reported in Yamada et al. (2017), $v_0 \approx 1\,\mathrm{mm\,h^{-1}}$ and use the typical cell size reported in Brown & Bron (1987), $2\ell = 13\mu\mathrm{m}$. With these numbers, our model predicts a typical extrusion energy on the order of

$$12 V_0 \approx 12 \times 6\pi\mu\ell^2 v_0 \approx 2 \times 10^{-13}\,\mathrm{J}. \tag{S9}$$

The factor of $12 = 2 \times 6$ is due to the hexagonal structure of the cell sheet. Note that our estimate of the extrusion energy is consistent with the finding in Yamada et al. (2017) for epithelial cell extrusion. Here, an actomyosin ring is measured to exhibit a contraction force of the order of $1\mathrm{kPa}$, which results in an extrusion energy of the order $1\mathrm{kPa} \times \ell^3 \approx 3 \times 10^{-13}\,\mathrm{J}$.

With these identifications of parameters, it is possible to extract dimensionful quantities from our simulations. This is what allows for e.g. the computation of cell cycle lengths in Fig 4.

We anticipate that the values of the couplings λ_i can be estimated from the extent and speed of CE (e.g in our model these would be determined by the values of λ_3 relative to λ_1).

Modeling neurulation/wrapping

The starting point for our simulation of neurulation is a planar sheet of cells where a line with a width of six cell radii is given non-zero wedging strength $|\alpha| = \alpha_0 > 0$ and all other cells have $\alpha = 0$. The line is centered at $x = 0$ and PCP is initialized orthogonally to this line, along the x direction ($\mathbf{q}|_{t=0} = \hat{\mathbf{x}}$). See Figure S4.

Cell proliferation is simulated as a Poisson process by choosing a rate Γ for *each cell* to divide in each time unit. Only cells at the neuroepithelium-ectoderm boundary (defined as cells with $|\alpha| > 0$ who are neighbours of cells with $\alpha = 0$) proliferate (with rate $\Gamma = \Gamma_0 > 0$) while the rest have $\Gamma = 0$. Daughter cells inherit all properties of their mother cell and are initiated randomly in a distance of one cell radius from their mother cell.

It should be noted that the initial width of the strip is not particularly important, since wedging will ensure the correct tube width given sufficient proliferation.

All cells in the simulation have the same coupling constants, typically $\lambda = (0.6, 0.4, 0)$. Typical values for Γ_0 and α_0 are 2.8×10^{-4} and 0.5. respectively.

Modeling gastrulation

In our gastrulation simulation, the assignment of PCP and cell wedging is characterized by two radii, describing an annulus (see Figure S5):

$$r_0 = 7, \tag{S10}$$

$$r_1 = 3r_0 = 21. \tag{S11}$$

PCP is assigned within the disk Ω_1 given by

$$\Omega_1 = \left\{ (x, y, z) \left| \sqrt{x^2 + y^2} < r_1 \right. \right\}. \tag{S12}$$

The PCP coupling strength λ is taken to be

$$\lambda = \begin{cases} (0.5, 0.5 - \lambda_3, \lambda_3) & \text{inside } \Omega_1, \\ (1, 0, 0) & \text{everywhere else.} \end{cases} \tag{S13}$$

where a typical value for λ_3 is between 0.08 and 0.12.

The PCP vector field $\mathbf{q}$ is initially assigned so that it spirals around the axis of tube formation (the z-axis):

$$\mathbf{q}|_{t=0} = \hat{\mathbf{z}} \times \mathbf{r}, \tag{S14}$$

In the gastrulation simulations, the PCP vector field is fixed on a per-cell basis.

Nonzero apical constriction parameter α is assigned in an annulus Ω_2, which shares its outer radius with the disk Ω_1:

$$\Omega_2 = \left\{ (x, y, z) \left| r_0 < \sqrt{x^2 + y^2} < r_1 \right. \right\}. \tag{S15}$$

The magnitude of α for the cells in Ω_2 is taken as 0.4:

$$|\alpha| = \begin{cases} 0.4 & \text{inside } \Omega_2, \\ 0 & \text{everywhere else.} \end{cases} \tag{S16}$$

The regions Ω_1 and Ω_2 are fixed in space and not on a particle basis. The number of particles in this simulation is $N = 4000$.

Modeling budding from plane

The budding simulation is, apart from global topology, very similar to the gastrulation simulation.

The relevant length parameters are r_0 and r_1 with $r_0 < r_1$. Typically we take

$$r_0 = 5, \tag{S17}$$

$$r_1 = 2r_0 \text{ or } r_1 = 3r_0. \tag{S18}$$

Two regions are correspondingly defined – the disk Ω_1 and the annulus Ω_2:

$$\Omega_1 := \left\{ (x, y, z) \left| \sqrt{x^2 + y^2} < r_1 \right. \right\}, \tag{S19}$$

$$\Omega_2 := \left\{ (x, y, z) \left| r_0 < \sqrt{x^2 + y^2} < r_1 \right. \right\}. \tag{S20}$$

The PCP coupling strength λ is taken to be

$$\lambda = \begin{cases} (0.5, 0.5 - \lambda_3, \lambda_3) & \text{inside } \Omega_1, \\ (1, 0, 0) & \text{everywhere else.} \end{cases} \tag{S21}$$

where a typical value for λ_3 is between 0.08 and 0.12.

The PCP vector field $\mathbf{q}$ is initially assigned so that it spirals around the center of invagination (the origin of coordinates):

$$\mathbf{q}|_{t=0} = \hat{\boldsymbol{z}} \times \mathbf{r}, \tag{S22}$$

In the gastrulation simulations, the PCP vector field is fixed on a per-cell basis.

Nonzero apical constriction parameter α is assigned in the annulus Ω_2 with magnitude 0.5:

$$|\alpha| = \begin{cases} 0.5 & \text{inside } \Omega_2, \\ 0 & \text{everywhere else.} \end{cases} \tag{S23}$$

The total number of particles in the simulation is 1384.

References

Brown, N. & Bron, A. J. (1987), 'An estimate of the human lens epithelial cell size in vivo', *Experimental Eye Research* **44**(6), 899–906.

Eskandari, H. & Salcudean, S. E. (2008), Characterization of the viscosity and elasticity in soft tissue using dynamic finite elements, *in* '2008 30th Annual International Conference of the IEEE Engineering in Medicine and Biology Society', IEEE, pp. 5573–5576.

Nielsen, B. F. (2019), 'OrganogenesisPCP',
https://github.com/BjarkeFN/OrganogenesisPCP.

Nissen, S. B., Rønhild, S., Trusina, A. & Sneppen, K. (2018), 'Theoretical tool bridging cell polarities with development of robust morphologies', *eLife* **7**, e38407.

Paszke, A., Gross, S., Chintala, S., Chanan, G., Yang, E., DeVito, Z., Lin, Z., Desmaison, A., Antiga, L. & Lerer, A. (2017), 'Automatic differentiation in pytorch'.

Sanchez-Corrales, Y. E., Blanchard, G. B. & Röper, K. (2018), 'Radially patterned cell behaviours during tube budding from an epithelium', *eLife* **7**, e35717.

Yamada, S., Iino, T., Bessho, Y., Hosokawa, Y. & Matsui, T. (2017), 'Quantitative analysis of mechanical force required for cell extrusion in zebrafish embryonic epithelia', *Biology Open* **6**(10), 1575–1580.